Journal of Materials Chemistry C

PAPER

View Article Online
View Journal | View Issue

Cite this: J. Mater. Chem. C, 2015, 3, 8839

Received 11th June 2015,
Accepted 22nd July 2015

DOI: 10.1039/c5tc01718a

www.rsc.org/MaterialsC

Structural, optical, and electronic studies of wide-bandgap lead halide perovskites†

Riccardo Comin,‡[a] Grant Walters,‡[a] Emmanuel Sol Thibau,[b] Oleksandr Voznyy,[a] Zheng-Hong Lu[b] and Edward H. Sargent*[a]

We investigate the family of mixed Br/Cl organolead halide perovskites which enable light emission in the blue-violet region of the visible spectrum. We report the structural, optical and electronic properties of this air-stable family of perovskites, demonstrating full bandgap tunability in the 400–550 nm range and enhanced exciton strength upon Cl substitution. We complement this study by tracking the evolution of the band levels across the gap, thereby providing a foundational framework for future optoelectronic applications of these materials.

Introduction

Organometallic lead halide thin films have been attracting an ever-growing interest from the photovoltaic scientific community following breakthroughs in solar-to-electric power conversion efficiencies,[1,2] which have recently risen to 20.1%[3] in a remarkably short timeframe. While the predominant research thrusts have since been oriented towards the use of these materials as active layers in light-harvesting devices, more recent studies have demonstrated optoelectronic applications of perovskite thin films in light-emitting-devices (LEDs),[4,5] lasers,[6–8] photodetectors,[9] and photocatalysts.[10] The physical chemistry of these compounds is particularly tolerant to mixed-halide synthesis,[2,11] which can lead to pure or mixed phases according to the structural compatibility of the different anions,[12–17] an aspect which is key to the impressive versatility characterizing this class of materials. While wide-bandgap perovskites are not suitable for photovoltaic applications due to their transparency to most of the solar spectrum, LED technology can fully leverage the optical tunability and spectral purity that can be simultaneously engineered in Br- and Cl-based lead halide perovskites. The optical tunability, in particular, is a direct consequence of the negative electronic compressibility of these systems, whereby a compression of the unit cell – implemented *via* anion substitution – can be used to increase the bandgap over a wide spectral range. In this context, recent studies have shown promising prospects for the use of lead halide perovskite films in light emission devices whose spectral response can be chemically tuned across the entire visible spectrum.[4,5] While extensive efforts are underway to optimize the efficiency of red and green perovskite LEDs, Cl-based films for blue-violet light emission have only been studied to a somewhat peripheral extent,[5,6] partly due to the lack of information on the electronic band levels. While earlier works have preliminarily addressed certain aspects of the near-gap bandstructure and related optical response in Cl- and Br-based thin films,[18,19] a detailed and systematic study of the electronic structure in the entire range of halide substitution is, to date, still lacking.

We therefore sought to shed light on the electronic structure of wide-bandgap $MAPbBr_{3-x}Cl_x$ thin film perovskites. Here we investigate the evolution of the structural and optical properties, as well as of the valence and conduction band levels, as a function of Cl/Br substitution using X-ray, optical, and photoelectron methods.

Results and discussion

For this study, we used solution processing routes to synthesize thin films of methylammonium (MA = CH_3NH_3) lead halide perovskite $MAPbBr_{3-x}Cl_x$ with Cl concentration values x = 0, 0.6, 1.2, 1.8, 2.4, 3 (see ESI,† for more details). For the pure-Cl compound, different chemical precursors have been used during synthesis, resulting in films showing no appreciable differences in the properties discussed hereafter (a comparison of the surface morphology is presented Fig. S1, ESI†).

Structural properties

For the study of structural properties we used X-ray diffraction (XRD), with corresponding scans shown in Fig. 1a. Multiple reflections can be seen that are associated with the cubic $Pm\bar{3}m$

[a] Department of Electrical and Computer Engineering, University of Toronto, 10 King's College Road, Toronto, Ontario, M5S 3G4, Canada. E-mail: ted.sargent@utoronto.ca
[b] Department of Materials Science and Engineering, University of Toronto, 184 College Street, Toronto, Ontario M5S 3E4, Canada

† Electronic supplementary information (ESI) available: Supplementary figures. See DOI: 10.1039/c5tc01718a

‡ These authors contributed equally.

space group. The lack of certain Bragg peaks for $x \geq 1.8$ is likely due to a higher degree of orientation in the film, confirmed by the presence of flat-lying cuboids in $MAPbCl_3$ (see again Fig. S1, ESI†). Most remarkably, we find a smooth evolution of the lattice structure across the entire concentration range, as demonstrated by the monotonic variation in the angular position of all Bragg reflections. The inset of Fig. 1a shows a zoomed view of the (001) Bragg peak as a function of x, which implies a contraction of the perovskite cage as the smaller anion Cl is substituted for Br. The cubic lattice constant a is extracted from the angular position of the (001) Bragg reflection θ_B using $\lambda/2a = \sin(\theta_B/2)$, and the average (shortest) grain dimension D is calculated from $D = 0.9\lambda/(\Delta\theta_B \cos\theta_B)$ where $\Delta\theta_B$ is the Bragg peak linewidth and λ is the X-ray wavelength (see Fig. S2, ESI†). The lattice constant is plotted in Fig. 1b together with the intensity of the Br-3d core levels measured with X-ray photoemission spectroscopy (XPS) (see also Fig. S3, ESI†). The monotonic trend in the lattice constant, which increases by ~5% from $MAPbBr_3$ to $MAPbCl_3$, confirms the progressive expansion of the unit cell. The variation over time of the sample structure and crystallinity is presented in Fig. 1c for the case of $MAPbCl_3$. The negligible evolution of the peak intensity and broadening combines with the absence of any sign of decomposition (inferred from the lack of peaks from the metal precursor $PbCl_2$) to provide evidence for an excellent structural stability in ambient conditions over more than 5 months.

Optical properties

We then proceeded to study the optical properties of $MAPbBr_{3-x}Cl_x$ films using absorption and photoluminescence (PL) spectroscopy. Fig. 2a shows a sequence of thin films on glass with compositions varying from pure Br- to pure Cl-perovskite, and where the change in the optical response is clearly discernible. The change in color indicates the increase in the bandgap as Br is replaced with Cl, consistent with the trend observed in the Br/I mixed halide perovskites,[20] and more generally expected due to the reduced covalency of the lead-halide bonds within the network of $Pb–X_6$ (X = Cl, Br, I) corner-sharing octahedra. Optical absorbance spectra, as well as PL scans, have been measured for films deposited on Spectrosil® substrates (the latter enable an extended spectral range of perovskite film investigation thanks to their high-energy absorption onset at $\lambda \sim 200$ nm) and are plotted in Fig. 2b. The gradual evolution in the absorption edge is consistent with the continuous structural change observed with XRD, while at the same time the excitonic pre-peak is found to increase in intensity, a behavior which is related to an increasing exciton binding strength as discussed in more detail below. Consistent with the high degree of stability seen using XRD, the optical response remains unaltered over extended periods of time and

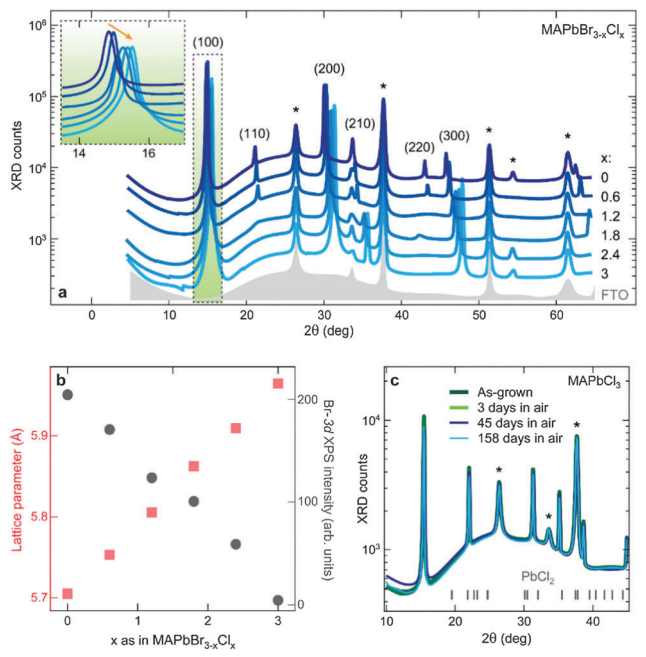

Fig. 1 (a) X-ray diffraction scans of $Pb(Ac)_2$-based thin films of $MAPbBr_{3-x}Cl_x$ (continuous lines) on fluorine-doped tin oxide (FTO). Shaded area: background signal from a pure FTO substrate (corresponding peaks are marked with a star). Inset: magnified view of the (100) diffraction peak. (b) Evolution of the lattice parameter and Br-3d peak intensity *vs.* x. (c) XRD pattern of $PbCl_2$-based $MAPbCl_3$ over time, demonstrating structural stability of pure-Cl films in atmosphere. The bottom bars mark the angular position of the powder XRD peaks in $PbCl_2$.

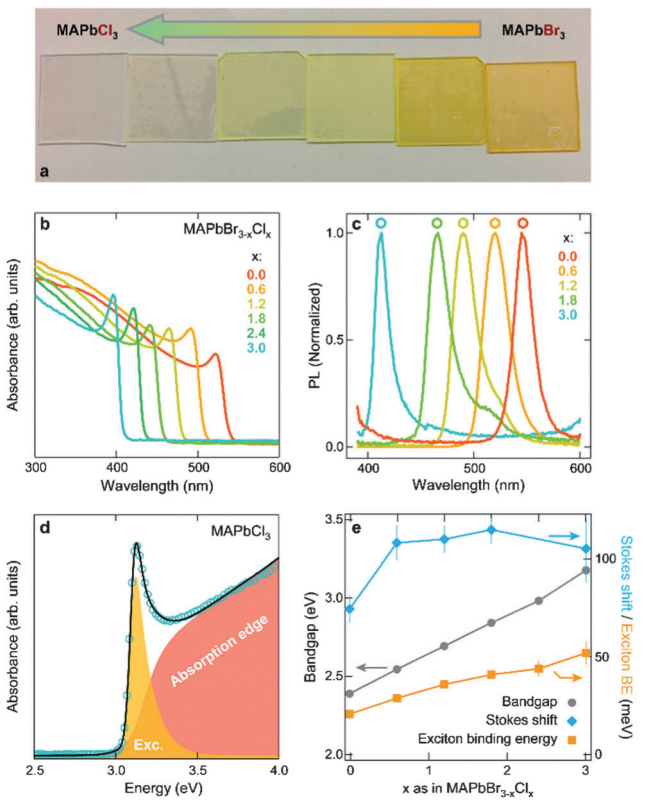

Fig. 2 (a) Photograph of Br/Cl mixed films on glass, visibly showing the progressive change in optical properties. (b and c) Optical absorbance and photoluminescence spectra (370 nm excitation) of $MAPbBr_{3-x}Cl_x$ films on Spectrosil®. (d) Plot of the absorbance (blue markers) of $MAPbCl_3$ as a function of energy with two-component (exciton and band-to-band absorption) fit overlaid (black line). (e) Evolution of the electronic bandgap (grey circles), Stokes shift (blue diamonds), and exciton binding energy (orange squares) as a function of Cl content x.

up to 1 month after fabrication (see Fig. S4, ESI†), confirming the overall stability of these materials in ambient conditions. Fig. 2c shows the normalized PL spectra, featuring a complementary progression in the emission wavelength, which blue-shifts from the green-emitting $MAPbBr_3$ to the deep-violet $MAPbCl_3$, thus confirming the controllable color tunability upon halogen substitution. The raw PL data, as well as the PL quantum efficiency (defined as the ratio of emitted to absorbed photons), are shown in Fig. S5, ESI.†

The absorbance profile, shown in Fig. 2d for the case of $MAPbCl_3$, is comprised of two main contributions: an excitonic peak at lower energies, and an extended absorption edge representing the continuum of valence-to-conduction band electronic excitations. Eqn (1) is used to model the excitonic absorption term using an asymmetric lineshape (to account for the higher-lying exciton levels as well as the interaction between the latter and the particle-hole continuum[21]) in the form of a hyperbolic secant:

$$\alpha_{exc}(E) = I_{exc} \cdot E^{-1} \times \left[\exp\left(\frac{E - E_{exc}}{\Gamma(E - E_{exc})}\right) + \exp\left(\frac{E_{exc} - E}{\Gamma(E - E_{exc})}\right)\right]^{-1} \quad (1)$$

where I_{exc} and E_{exc} represent the exciton intensity and energy respectively, and $\Gamma(E) = 2\Gamma_{exc}(1 + e^{aE})^{-1}$ is a generalized, energy-dependent linewidth. The exciton energy is related to the exciton binding energy G by $E_{exc} = E_g - G/n^2$ (E_g is the electronic bandgap) and here we use a single line corresponding to the exciton ground state (n = 1). For the main absorption edge, we use a modified version[22] of the canonical lineshape for direct transitions[23] (eqn (2)):

$$\alpha_{cont}(E) = I_{cont} \cdot \sqrt{G} \cdot E^{-1} \times \left[1 - \exp\left(-\pi\sqrt{G/E - E_G}\right)\right]^{-1} \cdot h(E) \times \theta(E - E_g) \quad (2)$$

where I_{cont} represents the intensity of the absorption edge, $\theta(E)$ is the Heaviside step function, and the function $h(E) = [1 - b(E - E_G)]^{-1}$ parametrizes the deviation from the parabolic band regime (following ref. 22). The expression for the absorption edge in eqn (1) is subsequently convoluted with a hyperbolic secant function with constant linewidth Γ_{cont}. The experimental data are fitted with the sum of the excitonic and continuum terms, and the resulting profile (together with the individual components) is shown in Fig. 2d (for the other compositions see Fig. S6, ESI†). In general, we make use of the fact that the same parameter G controls both the position of the exciton line and the lineshape of the main absorption edge to provide a reliable estimate for the bandgap as well as the exciton binding energy. The results for the bandgap, the Stokes shift (defined as $E_{exc} - E_{PL}$, where E_{PL} is the PL peak energy), and the exciton binding energy G are reported in Fig. 2e, as well as in Table S1 (ESI†). As already noted from the absorption spectra, G increases with Cl content, which reflects the more pronounced ionic character in Cl-based perovskites. In pure $MAPbCl_3$ we determine an exciton binding energy of about 50 meV, more than double the value for $MAPbBr_3$ ($G \sim 21$ meV), while in general our absolute values are compatible or slightly lower than previous optical studies on I-based perovskite.[22,24]

Electronic structure

In order to map the conduction and valence band levels as a function of halide content, we have further investigated the energetics of occupied states using Ultraviolet Photoemission Spectroscopy (UPS). Photoemission not only measures the binding energy (E_B) of valence electrons with respect to the chemical potential, but also provides a means for determining the work function (ϕ) of the material which sets the minimum kinetic energy (E_K) required for photoelectrons to escape the film according to $E_K = h\nu - \phi - |E_B|$, where $h\nu$ is the photon energy. Therefore, since E_K must be positive, a drop in the photoelectron signal in the form of an intensity cutoff occurs at $|E_B| = h\nu - \phi$, which is clearly visible in the photoelectron traces

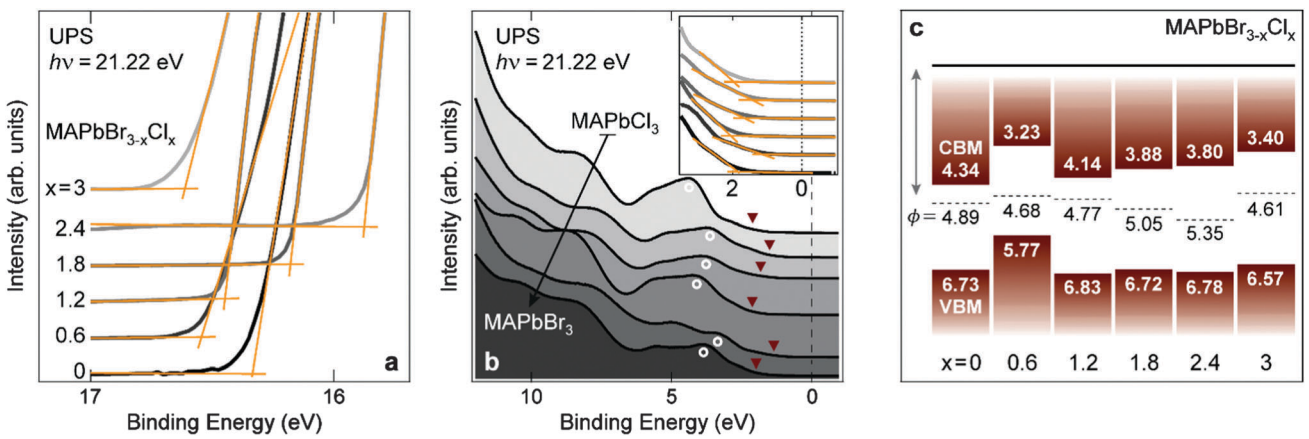

Fig. 3 (a) Low-energy secondary electron cutoff of $MAPbBr_{3-x}Cl_x$ films as measured using X-ray photoemission; arrows are located at the intersection between linear fits (orange traces) and mark the cutoff position in each spectrum. (b) Valence band photoemission spectra near the Fermi energy E_F with position of the valence band maximum pinned at the onset in the photoelectron signal as determined by linear fits (orange traces). In the main graph, red triangles and white circles mark the positions of the valence band onset and of the lowest-energy peak, respectively. (c) Schematics of the electronic structure of $MAPbBr_{3-x}Cl_x$ films across the gap, with work function (ϕ), valence band maximum (VBM), and conduction band minimum (CBM) values reported as the energy distance from the vacuum level.

shown in Fig. 3a, and measured using a UV source ($h\nu$ = 21.22 eV). Linear fits to the pre- and post-cutoff regions are used to estimate the energy onset from which the work function can be derived (values listed in Table S1, ESI†). The valence band photoemission spectra are displayed in Fig. 3b, with a magnified view near the Fermi level shown in the inset plot. Again, linear fits below and above the onset of the occupied density of states are used to locate the valence band maximum, as measured with respect to the Fermi energy E_F. The resulting band structure *vs.* Cl concentration is summarized in the schematic presented in Fig. 3c (all energies are referred to the vacuum level). A close inspection of this diagram leads to the following conclusions: (i) the pure-Br perovskite exhibits an ostensible asymmetry in the position of the band edges, consistent with previous findings;[25] (ii) when Cl is substituted for Br, the material develops a more intrinsic electronic structure, which might suggest a cleaner bandgap with lower defect density; (iii) for increasing Cl content, the valence band position shows little variation, while a monotonic trend is found for the conduction band edge (with the exception of x = 0.6); (iv) the work function does not follow a specific trend with halide substitution, and in all cases ranges around 5 eV.

Conclusions

Thin films of mixed-halide wide-bandgap perovskites reveal a number of interesting characteristics. Structural measurements show that Cl can be seamlessly substituted for Br, attributable to the lattice compatibility of the pure-halide compounds. The smooth structural evolution translates to a full tunability of optical properties, a behavior which enables the fabrication of spectrally-tunable lead halide perovskites having bandgaps in the 400 to 550 nm wavelength range. In light of the promising radiative performance of I-based perovskites,[4] the increased ionicity of Cl-containing perovskites suggests that the latter might represent a compelling platform for efficient, air-stable, light-emitting devices in the blue-violet region of the visible spectrum. Our photoemission results ultimately provide a comprehensive mapping of the electronic levels to guide future device design strategies in these materials.

Experimental

Synthesis of lead halide perovskite thin films

Metal salt precursors $Pb(Ac)_2$ (Ac = CH_3COO), $PbBr_2$ and $PbCl_2$ (99.999% purity) were purchased from Sigma Aldrich. The organic salt precursor CH_3NH_3Br (CH_3NH_3Cl) was synthesized by the reaction of methylamine aqueous solution and the corresponding hydrobromide (hydrochloride) acid in a round-bottom flask at 0 °C for 2 h with stirring. The precipitate was recovered by placing the solution on a rotary evaporator and carefully removing the solvents. The raw product CH_3NH_3X was re-dissolved in absolute ethanol and precipitated with the addition of diethyl ether for recrystallization. After filtration, the previous step was repeated again. Finally, the solid product was collected and dried at 60 °C in a vacuum oven for 24 h.

All substrates were chemically washed prior to film deposition. Substrates were immersed and sonicated in baths of Triton X-100 cleaning solution, isopropanol, and deionized water sequentially. After each bath, substrates were rinsed with deionized water. The substrates were then dried in an oven at 90 °C for 1.5 to 2 hours. This was followed by a final soak in an isopropanol bath for six hours and subsequent drying with nitrogen gas. After chemical washing, glass and Spectrosil® substrates were plasma treated for five minutes with an oxygen plasma in order to improve film wetting. Following plasma treatment, films were immediately deposited on the substrates using a one-step or a two-step method.

For one-step syntheses, lead precursor [$Pb(Ac)_2$, $PbBr_2$, or $PbCl_2$] and methylammonium halide were weighed and added together in a vial such that the molar ratio of lead to halide was 1 : 3. Solvent was then added to the powder precursors. For two-step syntheses, lead precursor and methylammonium halide were weighed out separately and solvent was added to each powder individually. Unless stated otherwise, dimethyl sulfoxide (DMSO) was used as the solvent and the concentration of Pb^{2+} was 0.6 M L^{-1} in all experiments. Solutions were vortexed and then sonicated for ~20 min. For one-step syntheses, 150 μL of solution were deposited on clean substrates for spin-coating. Samples were spun at 4000 rpm for 1 minute. For two-step syntheses, ten drops of lead precursor solution were spun using the same procedure; spin coating was then repeated with ten drops of methylammonium halide solution. In the case of anti-solvent rapid crystallization, a 50 μL aliquot of chlorobenzene was deposited onto the spinning sample after spinning at 10 000 rpm for 10 seconds and 30 seconds at 5000 rpm; spinning was continued for 30 seconds at 5000 rpm after chlorobenzene addition. All samples were immediately annealed for 45 minutes at 100 °C on a hotplate. The entire fabrication procedure was performed in a room-temperature nitrogen atmosphere.

Characterization of perovskite thin films

X-ray diffraction (XRD). XRD scans have been acquired on a Rigaku MiniFlex 600 diffractometer equipped with a NaI scintillation counter and using monochromatized Cu-K_α radiation (λ = 1.5406 Å), with a detector angle (2θ) step of 0.03°. The angular resolution is $\Delta_{2\theta}$ ~ 0.1°, as determined from diffraction on LaB_6 single crystals.

X-ray photoelectron spectroscopy (XPS). The Cl concentration values in mixed Br/Cl perovskite films have been obtained from the analysis of XPS spectra. The latter have been measured using a PHI-5500 setup using a monochromatized Al-K_α x-ray anode (1486.7 eV) to excite photoelectrons in an ultrahigh vacuum atmosphere (~10^{-9} Torr).

Scanning electron microscopy (SEM). A Quanta FEG 250 environmental scanning electron microscope was used to collect SEM images. Images were acquired with an Everhart–Thornley secondary electron detector, under high vacuum, and with a 10.0 kV accelerating voltage. Cross-sectional samples were lightly carbon-coated prior to imaging in order to prevent sample charging.

Optical absorption. optical absorption scans have been acquired with a Perkin Elmer Lambda 950 UV/Vis/NIR spectrophotometer equipped with a 150 mm integrating sphere, in the wavelength range 250–900 nm and using 2 nm incremental steps.

Photoluminescence (PL) spectra. PL emission profiles have been measured using a Horiba Fluorolog setup equipped with a monochromatized Xe lamp and with a photon detection unit featuring a double-grating spectrometer and a photomultiplier tube covering the spectral range 300–850 nm. All PL datasets have been acquired using λ = 370 nm excitation and in reflection geometry (at an incidence angle of 30° from the sample surface, to avoid spurious reflections of the incident light into the spectrometer). The raw data have been subsequently corrected for the experimentally-determined spectral sensitivity of the photon detector.

Ultraviolet photoemission spectroscopy (UPS)

Photoelectron Spectroscopy (PES) was performed in a PHI5500 Multi-Technique system using monochromatic Al-K_α radiation (XPS, $h\nu$ = 1486.7 eV) and non-monochromatized He-I_α radiation (UPS, $h\nu$ = 21.22 eV). All workfunction and valence band measurements were performed at a take-off angle of 88 degrees, and the chamber pressure was approximately 10^{-9} Torr. During measurement, the sample was held at a constant bias of −15 V relative to the spectrometer in order to improve the low energy photoelectron signal. Note that the samples have been exposed to atmosphere for a brief period of time (~5 minutes) in order to apply carbon-tape conductive contacts to the films (to avoid charging effects) prior to loading into the photoemission chamber.

Acknowledgements

This publication is based in part on work supported by Award KUS-11-009-21, made by the King Abdullah University of Science and Technology (KAUST), by the Ontario Research Fund Research Excellence Program, and by the Natural Sciences and Engineering Research Council.

Notes and references

1 J. Burschka, N. Pellet, S. J. Moon, R. Humphry-Baker, P. Gao, M. K. Nazeeruddin and M. Grätzel, *Nature*, 2013, **499**, 316–319.
2 M. Liu, M. B. Johnston and H. J. Snaith, *Nature*, 2013, **501**, 395–398.
3 W. S. Yang, J. H. Noh, N. J. Jeon, Y. C. Kim, S. Ryu, J. Seo and S. I. Seok, *Science*, 2015, aaa9272.
4 Z. K. Tan, R. S. Moghaddam, M. L. Lai, P. Docampo, R. Higler, F. Deschler, M. Price, A. Sadhanala, L. M. Pazos, D. Credgington, F. Hanusch, T. Bein, H. J. Snaith and R. H. Friend, *Nat. Nanotechnol.*, 2014, **9**, 687–692.
5 Y.-H. Kim, H. Cho, J. H. Heo, T.-S. Kim, N. Myoung, C.-L. Lee, S. H. Im and T.-W. Lee, *Adv. Mater.*, 2015, **27**, 1248–1254.
6 G. Xing, N. Mathews, S. S. Lim, N. Yantara, X. Liu, D. Sabba, M. Grätzel, S. Mhaisalkar and T. C. Sum, *Nat. Mater.*, 2014, **13**, 476–480.
7 F. Deschler, M. Price, S. Pathak, L. E. Klintberg, D.-D. Jarausch, R. Higler, S. Hüttner, T. Leijtens, S. D. Stranks, H. J. Snaith, M. Atatüre, R. T. Phillips and R. H. Friend, *J. Phys. Chem. Lett.*, 2014, **5**, 1421–1426.
8 B. R. Sutherland, S. Hoogland, M. M. Adachi, C. T. O. Wong and E. H. Sargent, *ACS Nano*, 2014, **8**, 10947–10952.
9 L. Dou, Y. (Micheal) Yang, J. You, Z. Hong, W.-H. Chang, G. Li and Y. Yang, *Nat. Commun.*, 2014, **5**, 5404.
10 J. Luo, J.-H. Im, M. T. Mayer, M. Schreier, M. K. Nazeeruddin, N.-G. Park, S. D. Tilley, H. J. Fan and M. Grätzel, *Science*, 2014, **345**, 1593–1596.
11 S. D. Stranks, G. E. Eperon, G. Grancini, C. Menelaou, M. J. P. Alcocer, T. Leijtens, L. M. Herz, A. Petrozza and H. J. Snaith, *Science*, 2013, **342**, 341–344.
12 K. Yamada, K. Nakada, Y. Takeuchi, K. Nawa and Y. Yamane, *Bull. Chem. Soc. Jpn.*, 2011, **84**, 926–932.
13 E. Mosconi, A. Amat, M. K. Nazeeruddin, M. Grätzel and F. De Angelis, *J. Phys. Chem. C*, 2013, **117**, 13902–13913.
14 S. Colella, E. Mosconi, P. Fedeli, A. Listorti, F. Gazza, F. Orlandi, P. Ferro, T. Besagni, A. Rizzo, G. Calestani, G. Gigli, F. De Angelis and R. Mosca, *Chem. Mater.*, 2013, **25**, 4613–4618.
15 E. Edri, S. Kirmayer, M. Kulbak, G. Hodes and D. Cahen, *J. Phys. Chem. Lett.*, 2014, **5**, 429–433.
16 B. Suarez, V. Gonzalez-Pedro, T. S. Ripolles, R. S. Sanchez, L. Otero and I. Mora-Sero, *J. Phys. Chem. Lett.*, 2014, **5**, 1628–1635.
17 S. Colella, E. Mosconi, G. Pellegrino, A. Alberti, V. L. P. Guerra, S. Masi, A. Listorti, A. Rizzo, G. G. Condorelli, F. De Angelis and G. Gigli, *J. Phys. Chem. Lett.*, 2014, **5**, 3532–3538.
18 N. Kitazawa, Y. Watanabe and Y. Nakamura, *J. Mater. Sci.*, 2002, **37**, 3585–3587.
19 M. Zhang, H. Yu, M. Lyu, Q. Wang, J.-H. Yun and L. Wang, *Chem. Commun.*, 2014, **50**, 11727–11730.
20 J. H. Noh, S. H. Im, J. H. Heo, T. N. Mandal and S. I. Seok, *Nano Lett.*, 2013, **13**, 1764–1769.
21 C. Bellabarba, J. Gonzalez and C. Rincon, *Phys. Rev. B: Condens. Matter Mater. Phys.*, 1996, **53**, 7792–7796.
22 M. Saba, M. Cadelano, D. Marongiu, F. Chen, V. Sarritzu, N. Sestu, C. Figus, M. Aresti, R. Piras, A. G. Lehmann, C. Cannas, A. Musinu, F. Quochi, A. Mura and G. Bongiovanni, *Nat. Commun.*, 2014, **5**, 5049.
23 R. J. Elliott, *Phys. Rev.*, 1957, **108**, 1384–1389.
24 V. D'Innocenzo, G. Grancini, M. J. P. Alcocer, A. R. S. Kandada, S. D. Stranks, M. M. Lee, G. Lanzani, H. J. Snaith and A. Petrozza, *Nat. Commun.*, 2014, **5**, 3586.
25 P. Schulz, E. Edri, S. Kirmayer, G. Hodes, D. Cahen and A. Kahn, *Energy Environ. Sci.*, 2014, **7**, 1377–1381.

Journal of
Materials Chemistry C

CORRECTION

View Article Online
View Journal | View Issue

Cite this: J. Mater. Chem. C, 2015, 3, 9480

Correction: Structural, optical, and electronic studies of wide-bandgap lead halide perovskites

Riccardo Comin,[a] Grant Walters,[a] Emmanuel Sol Thibau,[b] Oleksandr Voznyy,[a] Zheng-Hong Lu[b] and Edward H. Sargent*[a]

DOI: 10.1039/c5tc90155c

www.rsc.org/MaterialsC

Correction for 'Structural, optical, and electronic studies of wide-bandgap lead halide perovskites' by Riccardo Comin *et al.*, *J. Mater. Chem. C*, 2015, **3**, 8839–8843.

There are two errors on the second page of this article. The first concerns the sentence "The monotonic trend in the lattice constant, which increases by ~5% from $MAPbBr_3$ to $MAPbCl_3$, confirms the progressive expansion of the unit cell." which should read "The monotonic trend in the lattice constant, which increases by ~5% from **$MAPbCl_3$ to $MAPbBr_3$**, confirms the progressive expansion of the unit cell." The second error concerns the plot in Fig. 1b, the correct version of this figure is as follows:

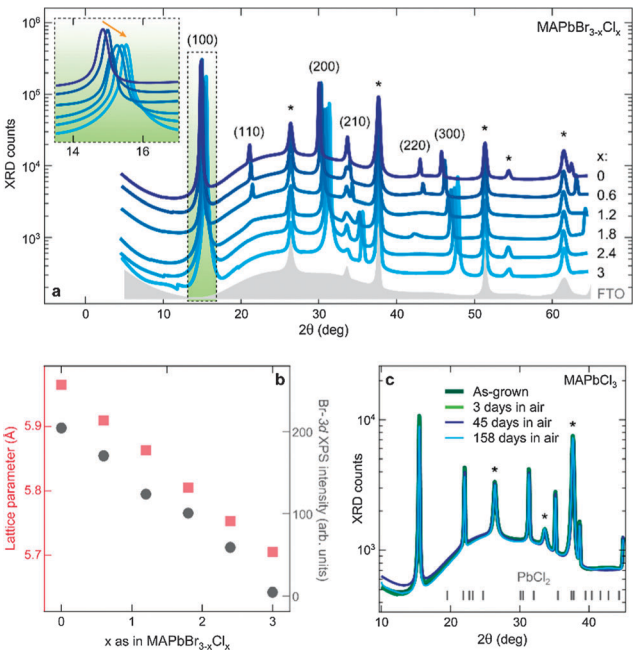

Fig. 1 (a) X-ray diffraction scans of $Pb(Ac)_2$-based thin films of $MAPbBr_{3-x}Cl_x$ (continuous lines) on fluorine-doped tin oxide (FTO). Shaded area: background signal from a pure FTO substrate (corresponding peaks are marked with a star). Inset: magnified view of the (100) diffraction peak. (b) Evolution of the lattice parameter and Br-3d peak intensity *vs.* *x*. (c) XRD pattern of $PbCl_2$-based $MAPbCl_3$ over time, demonstrating structural stability of pure-Cl films in ambient conditions. The bottom bars mark the angular position of the powder XRD peaks in $PbCl_2$.

The Royal Society of Chemistry apologises for these errors and any consequent inconvenience to authors and readers.

[a] *Department of Electrical and Computer Engineering, University of Toronto, 10 King's College Road, Toronto, Ontario, M5S 3G4, Canada. E-mail: ted.sargent@utoronto.ca*
[b] *Department of Materials Science and Engineering, University of Toronto, 184 College Street, Toronto, Ontario M5S 3E4, Canada*